Energy levels of ABC-stacked trilayer graphene quantum dots with infinite-mass boundary conditions

M. Mirzakhani,[1,2,*] M. Zarenia,[1,†] D. R. da Costa,[1,3,‡] S. A. Ketabi,[2,§] and F. M. Peeters[1,3,‖]

[1]*Department of Physics, University of Antwerp, Groenenborgerlaan 171, B-2020 Antwerp, Belgium*
[2]*School of Physics, Damghan University, P. O. Box 36716-41167, Damghan, Iran*
[3]*Departamento de Física, Universidade Federal do Ceará, 60455-900 Fortaleza, Ceará, Brazil*

Using the continuum model, we investigate the confined states and the corresponding wave functions of ABC-stacked trilayer graphene (TLG) quantum dots (QDs). First, a general infinite-mass boundary condition is derived and applied to calculate the electron and hole energy levels of a circular QD in both the absence and presence of a perpendicular magnetic field. Our analytical results for the energy spectra agree with those obtained by using the tight-binding model, where a TLG QD is surrounded by a staggered potential. Our findings show that (*i*) the energy spectrum exhibits intervalley symmetry $E_K^e(m) = -E_{K'}^h(m)$ for the electron (e) and hole (h) states, where m is the angular momentum quantum number, (*ii*) the zero-energy Landau level (LL) is formed by the magnetic states with $m \leq 0$ for both Dirac valleys, that is different from monolayer and bilayer graphene QD with infinite-mass potential in which only one of the cones contributes, and (*iii*) groups of three quantum Hall edge states in the tight-binding magnetic spectrum approach the zero LL, which results from the layer symmetry in TLG QDs.

I. INTRODUCTION

Since the discovery of graphene, a single atomic-thin layer of graphite, there has been significant progress in the realization of graphene quantum dots (QDs) and the investigation of their electronic, optical and transport properties [1–11]. Nanolithography of a graphene sheet is the most popular approach to fabricate monolayer graphene (MLG) QDs with possible applications as single-electron transistors and supersensitive electrometry [12,13]. Such QDs demonstrate size- and edge-dependent properties which are quite distinct from traditional semiconductor QDs.

Additionally, bilayer graphene (BLG) QDs have also attracted major interest and display desirable properties for applications [14–20]. In contrast to MLG QDs which are fabricated by direct etching of a graphene sheet, BLG QDs can be realized using local electrostatic gate potentials [14,15] and therefore the influence of edges is no longer important. In addition, energy levels of BLG flakes with different geometries and edge terminations have been recently addressed [16,17,21,22]. The weak interlayer coupling in BLG QDs exert a significant influence on the energy levels leading to new properties distinct from those of MLG QDs. Therefore, it will be interesting to investigate how the interlayer coupling in graphene QDs with three or more stacked layers exhibit different properties from BLG and MLG QDs. Despite the considerable number of studies on MLG and BLG QDs, there is, to our knowledge, no theoretical study on QDs in *trilayer* graphene (TLG). TLG

QDs, similar to MLG and BLG QDs, can be fabricated using etching techniques from exfoliated samples [23,24].

The electronic properties of graphene QDs can be described by either a tight-binding model (TBM) or by a continuum approach [10] (i.e., solving the two dimensional Dirac equation). Applying appropriate boundary conditions in the continuum model, the results are expected to be equivalent with those from a tight-binding approach in case of large sizes and low energies. Nearly 30 years ago, Berry and Modragon derived *infinite-mass* boundary condition for the confinement of neutrinos in a hard-wall billiard described by the Dirac-Weyl equation [25]. The main advantages of this model are that (*i*) analytic results can be obtained and (*ii*) that the results are comparable [26,27] to the tight-binding results for low energies and for particular edge termination. The infinite-mass boundary condition was previously employed to investigate the energy levels of both MLG [8,27,28] and BLG QDs [19]. However, at present there exist no derivation of the infinite-mass boundary condition for TLG and no investigation of the energy levels in such TLG QDs.

In this paper, by solving the Dirac-Weyl equation, we obtain the energy levels of a circular QDs in ABC-stacked TLG. A schematic picture of our system is shown in Fig. 1. First we derive the infinite-mass boundary condition for TLG. Confinement by a local mass term, which can be induced by the substrate, in the Dirac equation opens an energy gap between the electron and hole levels regardless of the shape of the dot. To complement our study, we compare our analytical results with the energy levels of a TLG QD surrounded by a mass potential media using the tight-binding approach.

The outline of this paper is as follows. In Sec. II, we derive the infinite-mass boundary condition of the Dirac equation for TLG which can be used for any dot geometry in TLG. In Secs. III and IV, we use this infinite-mass boundary condition and solve the Dirac-Weyl equation for a circular TLG QD in both the absence and the presence of an external perpendicular

———————
*mohammad.mirzakhani@uantwerpen.be
†mohammad.zarenia@uantwerpen.be
‡diego_rabelo@fisica.ufc.br
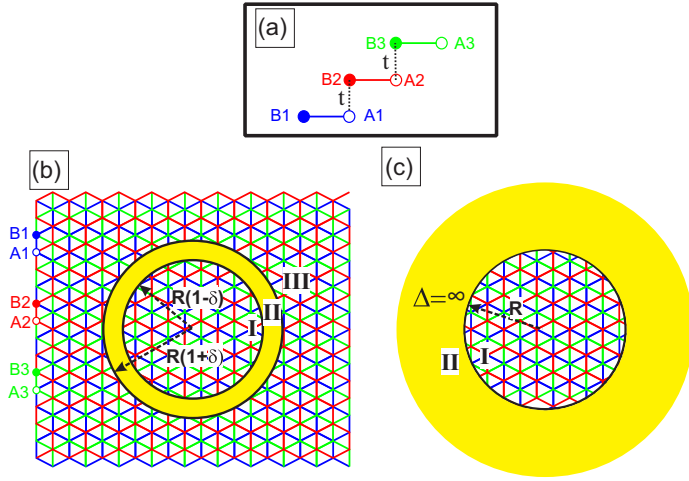§saketabi@du.ac.ir
‖francois.peeters@uantwerpen.be

FIG. 1. Schematic pictures of (a) couplings for ABC stacking in TLG, the mass potential for (b) ring-shaped barrier, and (c) dot barrier. Yellow region indicates the mass potential barrier.

magnetic field. We compare our results with those from the tight-binding approach obtained for a circular TLG dot surrounded by a staggered potential in Sec. V. We conclude in Sec. VI.

II. INFINITE-MASS BOUNDARY CONDITION

Here we will generalize the infinite-mass boundary condition that was previously formulated for MLG [8,27,28] and BLG [19] to TLG. The dynamics of carriers in ABC-stacked TLG in the presence of a circular mass barrier can be described by [29–36]

$$
\mathcal{H} = \begin{pmatrix}
\tau\Delta & \pi & t & 0 & 0 & 0 \\
\pi^\dagger & -\tau\Delta & 0 & 0 & 0 & 0 \\
t & 0 & \tau\Delta & \pi^\dagger & 0 & 0 \\
0 & 0 & \pi & -\tau\Delta & 0 & t \\
0 & 0 & 0 & 0 & \tau\Delta & \pi \\
0 & 0 & 0 & t & \pi^\dagger & -\tau\Delta
\end{pmatrix}, \quad (1)
$$

with the momentum operators $\pi = p_x + ip_y$ and $\pi^\dagger = p_x - ip_y$ in polar coordinates

$$
\pi = -i\hbar v_F e^{i\theta}\left[\frac{\partial}{\partial r} + \frac{i}{r}\frac{\partial}{\partial \theta}\right], \quad (2)
$$

$$
\pi^\dagger = -i\hbar v_F e^{-i\theta}\left[\frac{\partial}{\partial r} - \frac{i}{r}\frac{\partial}{\partial \theta}\right], \quad (3)
$$

where $v_F \approx 10^6$ m/s is the velocity of the carriers in TLG, and r and θ are the radial and azimuthal coordinates, respectively. The two valleys are labeled by the quantum number τ, where $\tau = 1$ ($\tau = -1$) stands for the K (K') valley. $t \approx 400$ meV is the nearest-neighbor interlayer coupling term and Δ indicates a position-dependent mass term.

We note that, for TLG, the staggered potential induced by substrate might be smaller in the middle and top layers of TLG. However, in order to obtain analytical expression for the infinite-mass boundary conditions and further to compare the energy levels with tight-binding results (Sec. V), we employ a simplified structure for the mass potential profile, i.e., equal

potential strength in all layers, within our calculations of both continuum and tight-binding approaches. As an alternative experimental approach, one may sandwich the TLG by two substrates (i.e., one at the bottom and one on top). In this way the strength of the induced mass potential will be more uniform in all the layers. It is worth mentioning that the experimental realization of such two-dimensional heterostructures is practical within today's technology (e.g., see [37]). In fact, a substrate with different neighboring atoms, e.g., hexagonal boron nitride, is the appropriate substrate which can induce different mass potential on the neighboring carbon atoms, breaking the sublattice symmetry and thus opening an energy gap. However, in the case of ABC-stacked TLG, the configuration of the induced mass potential by the substrate is more complex: one may think that the A and B sublattices from the neighboring layers (dimer sites) must "feel" the same potential since they are on top of each other, but this implies a different potential between the dimer sites from the bottom and top layers. Here, we model a simplified configuration for the mass potential to open an energy gap and thus confinement in TLG.

We define the six-component wave function,

$$
\Psi = \begin{pmatrix}
e^{im\theta}\phi_{A1}(\rho) \\
ie^{i(m-1)\theta}\phi_{B1}(\rho) \\
e^{im\theta}\phi_{B2}(\rho) \\
ie^{i(m+1)\theta}\phi_{A2}(\rho) \\
e^{i(m+2)\theta}\phi_{A3}(\rho) \\
ie^{i(m+1)\theta}\phi_{B3}(\rho)
\end{pmatrix}, \quad (4)
$$

as the eigenstates of the Hamiltonian (1), where $m = 0, \pm 1, \pm 2, \ldots$ denotes the angular momentum label. The envelope functions $\phi_{A1}, \ldots, \phi_{B3}$ correspond to different sublattices $A1, \ldots, B3$, respectively. Solving the Schrödinger equation $\mathcal{H}\Psi = E\Psi$, the radial dependence of the wave function is determined by the following set of coupled differential equations:

$$
\left[\frac{\partial}{\partial\rho} - \frac{m-1}{\rho}\right]\phi_{B1}(\rho) = (\varepsilon - \tau\Delta')\phi_{A1}(\rho) - t'\phi_{B2}(\rho),
$$

$$
\left[\frac{\partial}{\partial\rho} + \frac{m}{\rho}\right]\phi_{A1}(\rho) = -(\varepsilon + \tau\Delta')\phi_{B1}(\rho),
$$

$$
\left[\frac{\partial}{\partial\rho} + \frac{m+1}{\rho}\right]\phi_{A2}(\rho) = (\varepsilon - \tau\Delta')\phi_{B2}(\rho) - t'\phi_{A1}(\rho), \quad (5)
$$

$$
\left[\frac{\partial}{\partial\rho} - \frac{m}{\rho}\right]\phi_{B2}(\rho) = -(\varepsilon + \tau\Delta')\phi_{A2}(\rho) + t'\phi_{B3}(\rho),
$$

$$
\left[\frac{\partial}{\partial\rho} - \frac{m+1}{\rho}\right]\phi_{B3}(\rho) = (\varepsilon - \tau\Delta')\phi_{A3}(\rho),
$$

$$
\left[\frac{\partial}{\partial\rho} + \frac{m+2}{\rho}\right]\phi_{A3}(\rho) = -(\varepsilon + \tau\Delta')\phi_{B3}(\rho) - t'\phi_{A2}(\rho),
$$

where the radial distance ρ is in units of the dot radius R. The dimensionless variables are $\varepsilon = E/E_0$, $t' = t/E_0$, and $\Delta' = \Delta/E_0$ with $E_0 = \hbar v_F/R$. In order to obtain the infinite-mass boundary condition, we solve Eqs. (5) inside the barrier region, $1 - \delta < \rho < 1 + \delta$ ($\delta \ll 1$), and apply the boundary conditions for the envelope functions at the boundaries, i.e., $\rho = 1 - \delta$ and $\rho = 1 + \delta$. This gives us the

following differential equations:

$$\frac{\partial}{\partial \rho}\phi_{B1} = -\tau\Delta'\phi_{A1} - t'\phi_{B2}, \quad \frac{\partial}{\partial \rho}\phi_{A1} = -\tau\Delta'\phi_{B1},$$

$$\frac{\partial}{\partial \rho}\phi_{A2} = -\tau\Delta'\phi_{B2} - t'\phi_{A1}, \quad \frac{\partial}{\partial \rho}\phi_{B2} = -\tau\Delta'\phi_{A2} + t'\phi_{B3},$$

$$\frac{\partial}{\partial \rho}\phi_{B3} = -\tau\Delta'\phi_{A3}, \quad \frac{\partial}{\partial \rho}\phi_{A3} = -\tau\Delta'\phi_{B3} + t'\phi_{A2}. \tag{6}$$

Decoupling the system of equations (6), we obtain the following differential equation for ϕ_{B3}:

$$\tau\left\{\frac{\partial^6}{\partial \rho^6} - 3\Delta'^2\frac{\partial^4}{\partial \rho^4} + (3\Delta'^4 - 2t'^2\Delta'^2)\frac{\partial^2}{\partial \rho^2}\right.$$

$$\left. + (-\Delta'^6 + 2\Delta'^4t'^2 - \Delta'^2t'^4)\right\}\phi_{B3} = 0. \tag{7}$$

Considering $Z = \partial^2/\partial \rho^2$, one can simplify the above equation as

$$\{Z^3 + \alpha_1 Z^2 + \alpha_2 Z + \alpha_3\}\phi_{B3} = 0, \tag{8}$$

where

$$\alpha_1 = -3\Delta'^2,$$

$$\alpha_2 = 3\Delta'^4 - 2t'^2\Delta'^2, \tag{9}$$

$$\alpha_3 = -\Delta'^6 + 2\Delta'^4 t'^2 - \Delta'^2 t'^4.$$

Equation (8) can be rewritten as

$$(Z - Z_1)(Z - Z_2)(Z - Z_3)\phi_{B3} = 0, \tag{10}$$

where Z_j ($j = 1,2,3$) are the three roots of the cubic equation. The spinor component ϕ_{B3} is a solution of

$$\frac{d^2\phi_{B3}}{d\rho^2} - \omega_j^2\phi_{B3} = 0, \tag{11}$$

where $\omega_j = \sqrt{Z_j}$. The solution for ϕ_{B3} reads

$$\phi_{B3} = Fe^{\omega_1(\rho-1)} + Ge^{-\omega_1(\rho-1)} + He^{\omega_2(\rho-1)} + Ie^{-\omega_2(\rho-1)}$$

$$+ Ke^{\omega_3(\rho-1)} + Le^{-\omega_3(\rho-1)}, \tag{12}$$

where F, G, H, I, K, and L are constants. The other spinor components can be obtained using Eqs. (6) as follows:

$$\phi_{A3} = -\frac{1}{\tau\Delta'}\{\omega_1 Fe^{\omega_1(\rho-1)} - \omega_1 Ge^{-\omega_1(\rho-1)} + \omega_2 He^{\omega_2(\rho-1)} - \omega_2 Ie^{-\omega_2(\rho-1)} + \omega_3 Ke^{\omega_3(\rho-1)} - \omega_3 Le^{-\omega_3(\rho-1)}\},$$

$$\phi_{A2} = -\frac{1}{\tau t'\Delta'}\{\Omega_1 Fe^{\omega_1(\rho-1)} + \Omega_1 Ge^{-\omega_1(\rho-1)} + \Omega_2 He^{\omega_2(\rho-1)} + \Omega_2 Ie^{-\omega_2(\rho-1)} + \Omega_3 Ke^{\omega_3(\rho-1)} + \Omega_3 Le^{-\omega_3(\rho-1)}\},$$

$$\phi_{A1} = \frac{\tau}{t'^2\Delta'}\{\gamma_1 Fe^{\omega_1(\rho-1)} - \gamma_1 Ge^{-\omega_1(\rho-1)} + \gamma_2 He^{\omega_2(\rho-1)} - \gamma_2 Ie^{-\omega_2(\rho-1)} + \gamma_3 Ke^{\omega_3(\rho-1)} - \gamma_3 Le^{-\omega_3(\rho-1)}\},$$

$$\phi_{B2} = \frac{1}{t'^3\Delta'^2}\{\Omega_1\gamma_1 Fe^{\omega_1(\rho-1)} - \Omega_1\gamma_1 Ge^{-\omega_1(\rho-1)} + \Omega_2\gamma_2 He^{\omega_2(\rho-1)} - \Omega_2\gamma_2 Ie^{-\omega_2(\rho-1)} + \Omega_3\gamma_3 Ke^{\omega_3^2(\rho-1)} - \Omega_3\gamma_3 Le^{-\omega_3(\rho-1)}\},$$

$$\phi_{B1} = -\frac{1}{t'^2\Delta'^2}\{\omega_1\gamma_1 Fe^{\omega_1(\rho-1)} + \omega_1\gamma_1 Ge^{-\omega_1(\rho-1)} + \omega_2\gamma_2 He^{\omega_2(\rho-1)} + \omega_2\gamma_2 Ie^{-\omega_2(\rho-1)} + \omega_3\gamma_3 Ke^{\omega_3(\rho-1)} + \omega_3\gamma_3 Le^{-\omega_3(\rho-1)}\}, \tag{13}$$

where $\gamma_j = (\omega_j^3 - 2\Delta'^2\omega_j + \frac{\Delta'^4 - t'^2\Delta'^2}{\omega_j})$ and $\Omega_j = (\omega_j^2 - \Delta'^2)$ with $j = 1,2,3$. These solutions at the boundary $\rho = 1 - \delta$ read

$$\phi_{A1}^{\mathrm{I}}(1-\delta) = \frac{\tau}{t'^2\Delta'}\{\gamma_1 Fe^{-\omega_1\delta} - \gamma_1 Ge^{\omega_1\delta} + \gamma_2 He^{-\omega_2\delta} - \gamma_2 Ie^{\omega_2\delta} + \gamma_3 Ke^{-\omega_3\delta} - \gamma_3 Le^{\omega_3\delta}\},$$

$$\phi_{B1}^{\mathrm{I}}(1-\delta) = -\frac{1}{t'^2\Delta'^2}\{\omega_1\gamma_1 Fe^{-\omega_1\delta} + \omega_1\gamma_1 Ge^{\omega_1\delta} + \omega_2\gamma_2 He^{-\omega_2\delta} + \omega_2\gamma_2 Ie^{\omega_2\delta} + \omega_3\gamma_3 Ke^{-\omega_3\delta} + \omega_3\gamma_3 Le^{\omega_3\delta}\},$$

$$\phi_{A2}^{\mathrm{I}}(1-\delta) = -\frac{1}{\tau t'\Delta'}\{\Omega_1 Fe^{-\omega_1\delta} + \Omega_1 Ge^{\omega_1\delta} + \Omega_2 He^{-\omega_2\delta} + \Omega_2 Ie^{\omega_2\delta} + \Omega_3 Ke^{-\omega_3\delta} + \Omega_3 Le^{\omega_3\delta}\}, \tag{14}$$

$$\phi_{B2}^{\mathrm{I}}(1-\delta) = \frac{1}{t'^3\Delta'^2}\{\Omega_1\gamma_1 Fe^{-\omega_1\delta} - \Omega_1\gamma_1 Ge^{\omega_1\delta} + \Omega_2\gamma_2 He^{-\omega_2\delta} - \Omega_2\gamma_2 Ie^{\omega_2\delta} + \Omega_3\gamma_3 Ke^{-\omega_3\delta} - \Omega_3\gamma_3 Le^{\omega_3\delta}\},$$

$$\phi_{A3}^{\mathrm{I}}(1-\delta) = -\frac{1}{\tau\Delta'}\{\omega_1 Fe^{-\omega_1\delta} - \omega_1 Ge^{\omega_1\delta} + \omega_2 He^{-\omega_2\delta} - \omega_2 Ie^{\omega_2\delta} + \omega_3 Ke^{-\omega_3\delta} - \omega_3 Le^{\omega_3\delta}\},$$

$$\phi_{B3}^{\mathrm{I}}(1-\delta) = Fe^{-\omega_1\delta} + Ge^{\omega_1\delta} + He^{-\omega_2\delta} + Ie^{\omega_2\delta} + Ke^{-\omega_3\delta} + Le^{\omega_3\delta},$$

and, at the other boundary $\rho = 1 + \delta$, become

$$\phi_{A1}^{\mathrm{III}}(1+\delta) = \frac{\tau}{t'^2\Delta'}\{\gamma_1 Fe^{\omega_1\delta} - \gamma_1 Ge^{-\omega_1\delta} + \gamma_2 He^{\omega_2\delta} - \gamma_2 Ie^{-\omega_2\delta} + \gamma_3 Ke^{\omega_3\delta} - \gamma_3 Le^{-\omega_3\delta}\},$$

$$\phi_{B1}^{\mathrm{III}}(1+\delta) = -\frac{1}{t'^2\Delta'^2}\{\omega_1\gamma_1 Fe^{\omega_1\delta} + \omega_1\gamma_1 Ge^{-\omega_1\delta} + \omega_2\gamma_2 He^{\omega_2\delta} + \omega_2\gamma_2 Ie^{-\omega_2\delta} + \omega_3\gamma_3 Ke^{\omega_3\delta} + \omega_3\gamma_3 Le^{-\omega_3\delta}\},$$

$$\phi_{A2}^{\mathrm{III}}(1+\delta) = -\frac{1}{\tau t'\Delta'}\{\Omega_1 Fe^{\omega_1\delta} + \Omega_1 Ge^{-\omega_1\delta} + \Omega_2 He^{\omega_2\delta} + \Omega_2 Ie^{-\omega_2\delta} + \Omega_3 Ke^{\omega_3\delta} + \Omega_3 Le^{-\omega_3\delta}\},$$

$$\phi_{B2}^{\mathrm{III}}(1+\delta) = \frac{1}{t'^3\Delta'^2}\{\Omega_1\gamma_1 Fe^{\omega_1\delta} - \Omega_1\gamma_1 Ge^{-\omega_1\delta} + \Omega_2\gamma_2 He^{\omega_2\delta} - \Omega_2\gamma_2 Ie^{-\omega_2\delta} + \Omega_3\gamma_3 Ke^{\omega_3\delta} - \Omega_3\gamma_3 Le^{-\omega_3\delta}\},$$

$$\phi_{A3}^{\mathrm{III}}(1+\delta) = -\frac{1}{\tau\Delta'}\{\omega_1 Fe^{\omega_1\delta} - \omega_1 Ge^{-\omega_1\delta} + \omega_2 He^{\omega_2\delta} - \omega_2 Ie^{-\omega_2\delta} + \omega_3 Ke^{\omega_3\delta} - \omega_3 Le^{-\omega_3\delta}\},$$

$$\phi_{B3}^{\mathrm{III}}(1+\delta) = Fe^{\omega_1\delta} + Ge^{-\omega_1\delta} + He^{\omega_2\delta} + Ie^{-\omega_2\delta} + Ke^{\omega_3\delta} + Le^{-\omega_3\delta}. \tag{15}$$

In the limit of $\delta \ll 1$ and by eliminating the coefficients F, G, H, I, K, and L, we obtain the following equations:

$$\frac{1}{\beta_{KL}}\big(\Xi_{KL}^{\mathrm{III}} - \Xi_{KL}^{\mathrm{I}}\big) = \frac{1}{\alpha_{KL}}\tanh(\omega_3\delta)\big(\Theta_{KL}^{\mathrm{III}} + \Theta_{KL}^{\mathrm{I}}\big),$$

$$\frac{1}{\beta_{HI}}\big(\Xi_{HI}^{\mathrm{III}} - \Xi_{HI}^{\mathrm{I}}\big) = \frac{1}{\alpha_{HI}}\tanh(\omega_2\delta)\big(\Theta_{HI}^{\mathrm{III}} + \Theta_{HI}^{\mathrm{I}}\big), \tag{16}$$

$$\frac{1}{\beta_{FG}}\big(\Xi_{FG}^{\mathrm{III}} - \Xi_{FG}^{\mathrm{I}}\big) = \frac{1}{\alpha_{FG}}\tanh(\omega_1\delta)\big(\Theta_{FG}^{\mathrm{III}} + \Theta_{FG}^{\mathrm{I}}\big),$$

where

$$\Xi_{KL}^{\mathrm{I}} = \frac{\omega_1\gamma_1}{\omega_1\gamma_1 - \omega_2\gamma_2}\left[\phi_{B3}^{\mathrm{I}}(1) + \frac{t'^2\Delta'^2}{\omega_1\gamma_1}\phi_{B1}^{\mathrm{I}}(1)\right] - \frac{\Omega_1}{(\omega_1^2 - \omega_2^2)}\left[\phi_{B3}^{\mathrm{I}}(1) + \frac{\tau t'\Delta'}{\Omega_1}\phi_{A2}^{\mathrm{I}}(1)\right], \tag{17a}$$

$$\Theta_{KL}^{\mathrm{I}} = \frac{\tau\omega_1\gamma_1}{\omega_1\gamma_2 - \omega_2\gamma_1}\left[\frac{t'^2\Delta'}{\gamma_1}\phi_{A1}^{\mathrm{I}}(1) + \frac{\Delta'}{\omega_1}\phi_{A3}^{\mathrm{I}}(1)\right] - \frac{\omega_1\gamma_1\Omega_1}{\omega_1\gamma_2\Omega_2 - \omega_2\gamma_1\Omega_1}\left[\frac{t'^3\Delta'^2}{\Omega_1\gamma_1}\phi_{B2}^{\mathrm{I}}(1) + \frac{\tau\Delta'}{\omega_1}\phi_{A3}^{\mathrm{I}}(1)\right], \tag{17b}$$

$$\Xi_{HI}^{\mathrm{I}} = \frac{\omega_1\gamma_1}{\omega_1\gamma_1 - \omega_3\gamma_3}\left[\phi_{B3}^{\mathrm{I}}(1) + \frac{t'^2\Delta'^2}{\omega_1\gamma_1}\phi_{B1}^{\mathrm{I}}(1)\right] - \frac{\Omega_1}{(\omega_1^2 - \omega_3^2)}\left[\phi_{B3}^{\mathrm{I}}(1) + \frac{\tau t'\Delta'}{\Omega_1}\phi_{A2}^{\mathrm{I}}(1)\right], \tag{17c}$$

$$\Theta_{HI}^{\mathrm{I}} = \frac{\tau\omega_1\gamma_1}{\omega_1\gamma_3 - \omega_3\gamma_1}\left[\frac{t'^2\Delta'}{\gamma_1}\phi_{A1}^{\mathrm{I}}(1) + \frac{\Delta'}{\omega_1}\phi_{A3}^{\mathrm{I}}(1)\right] - \frac{\omega_1\gamma_1\Omega_1}{\omega_1\gamma_3\Omega_3 - \omega_3\gamma_1\Omega_1}\left[\frac{t'^3\Delta'^2}{\Omega_1\gamma_1}\phi_{B2}^{\mathrm{I}}(1) + \frac{\tau\Delta'}{\omega_1}\phi_{A3}^{\mathrm{I}}(1)\right], \tag{17d}$$

$$\Xi_{FG}^{\mathrm{I}} = \frac{\omega_3\gamma_3}{\omega_3\gamma_3 - \omega_2\gamma_2}\left[\phi_{B3}^{\mathrm{I}}(1) + \frac{t'^2\Delta'^2}{\omega_3\gamma_3}\phi_{B1}^{\mathrm{I}}(1)\right] - \frac{\Omega_3}{(\omega_3^2 - \omega_2^2)}\left[\phi_{B3}^{\mathrm{I}}(1) + \frac{\tau t'\Delta'}{\Omega_3^2}\phi_{A2}^{\mathrm{I}}(1)\right], \tag{17e}$$

$$\Theta_{FG}^{\mathrm{I}} = \frac{\tau\omega_3\gamma_3}{\omega_3\gamma_2 - \omega_2\gamma_3}\left[\frac{t'^2\Delta'}{\gamma_1}\phi_{A1}^{\mathrm{I}}(1) + \frac{\Delta'}{\omega_3}\phi_{A3}^{\mathrm{I}}(1)\right] - \frac{\omega_3\gamma_3\Omega_3}{\omega_3\gamma_2\Omega_2 - \omega_2\gamma_3\Omega_3}\left[\frac{t'^3\Delta'^2}{\Omega_3\gamma_3}\phi_{B2}^{\mathrm{I}}(1) + \frac{\tau\Delta'}{\omega_3}\phi_{A3}^{\mathrm{I}}(1)\right], \tag{17f}$$

and

$$\alpha_{KL} = \frac{\omega_1\gamma_3 - \omega_3\gamma_1}{\omega_1\gamma_2 - \omega_2\gamma_1} - \frac{\omega_1\gamma_3\Omega_3 - \omega_3\gamma_1\Omega_1}{\omega_1\gamma_2\Omega_2 - \omega_2\gamma_1\Omega_1},$$

$$\beta_{KL} = \frac{\omega_1\gamma_1 - \omega_3\gamma_3}{\omega_1\gamma_1 - \omega_2\gamma_2} - \frac{\omega_1^2 - \omega_3^2}{\omega_1^2 - \omega_2^2},$$

$$\alpha_{HI} = \frac{\omega_1\gamma_2 - \omega_2\gamma_1}{\omega_1\gamma_3 - \omega_3\gamma_1} - \frac{\omega_1\gamma_2\Omega_2 - \omega_2\gamma_1\Omega_1}{\omega_1\gamma_3\Omega_3 - \omega_3\gamma_1\Omega_1}, \tag{18}$$

$$\beta_{HI} = \frac{\omega_1\gamma_1 - \omega_2\gamma_2}{\omega_1\gamma_1 - \omega_3\gamma_3} - \frac{\omega_1^2 - \omega_2^2}{\omega_1^2 - \omega_3^2},$$

$$\alpha_{FG} = \frac{\omega_3\gamma_1 - \omega_1\gamma_3}{\omega_3\gamma_2 - \omega_2\gamma_3} - \frac{\omega_3\gamma_1\Omega_1 - \omega_1\gamma_3\Omega_3}{\omega_3\gamma_2\Omega_2 - \omega_2\gamma_3\Omega_3},$$

$$\beta_{FG} = \frac{\omega_3\gamma_3 - \omega_1\gamma_1}{\omega_3\gamma_3 - \omega_2\gamma_2} - \frac{\omega_3^2 - \omega_1^2}{\omega_3^2 - \omega_2^2}.$$

The parameters Ξ_i^{III} (Θ_i^{III}) have the same form as Ξ_i^{I} (Θ_i^{I}) with the wave spinors given at the boundary III. Applying the limits $\delta \to 0$ and $\Delta' \gg t'$, respectively, for a thin and high mass barrier result in $\tanh(\omega_j\delta) = P = \mathrm{const}$ with $j = 1, 2, 3$, which allows us to rewrite Eqs. (16) as

$$\big(\Xi_{KL}^{\mathrm{III}} - \Xi_{KL}^{\mathrm{I}}\big) = P\big(\Theta_{KL}^{\mathrm{III}} + \Theta_{KL}^{\mathrm{I}}\big),$$

$$\big(\Xi_{HI}^{\mathrm{III}} - \Xi_{HI}^{\mathrm{I}}\big) = P\big(\Theta_{HI}^{\mathrm{III}} + \Theta_{HI}^{\mathrm{I}}\big), \tag{19}$$

$$\big(\Xi_{FG}^{\mathrm{III}} - \Xi_{FG}^{\mathrm{I}}\big) = P\big(\Theta_{FG}^{\mathrm{III}} + \Theta_{FG}^{\mathrm{I}}\big).$$

These are the boundary conditions for the general case shown in Fig. 1(b). Using these boundary conditions, we obtain the boundary conditions for a dot-shaped mass barrier shown in Fig. 1(c). In this case we take the limits

$$\Delta' = \infty, \quad P = 1,$$

$$\phi_{A1}^{\mathrm{III}} = \phi_{B1}^{\mathrm{III}} = \phi_{A2}^{\mathrm{III}} = \phi_{B2}^{\mathrm{III}} = \phi_{A3}^{\mathrm{III}} = \phi_{B3}^{\mathrm{III}} = 0, \tag{20}$$

and the boundary conditions (19) simplify to

$$\tau\phi_{A1}^{\mathrm{I}}(1) + \phi_{B1}^{\mathrm{I}}(1) = 0,$$

$$\tau\phi_{A2}^{\mathrm{I}}(1) - \phi_{B2}^{\mathrm{I}}(1) = 0, \tag{21}$$

$$\tau\phi_{A3}^{\mathrm{I}}(1) + \phi_{B3}^{\mathrm{I}}(1) = 0.$$

By analyzing the infinite-mass boundary condition formed by a set of three equations (21), we notice that (*i*) the three relations have the same structure except for some sign changes, (*ii*) each equation of the boundary conditions connects the value of the pseudospin components in the same layer (i.e., $A1 - B1$, $A2 - B2$, and $A3 - B3$), (*iii*) the boundary condition involve only the wave functions in region I, that is consistent with the fact that the charge carries are forbidden to move outside the dot, i.e., region II, and (*iv*) similar to the BLG QD case, the boundary condition does not connect the wave function components from different layers. Within the next sections, we will calculate the energy spectrum both in the absence (Sec. III) and in the presence (Sec. IV) of an

external magnetic field for circular QDs in TLG using the obtained boundary conditions [Eq. (21)].

III. TLG QD: ZERO MAGNETIC FIELD

In the case of zero magnetic field $B = 0$, the radial dependence of the wave function is given by Eqs. (5) except that $\Delta' = 0$. The effect of the infinity mass potential Δ' is now expressed by the boundary conditions (21). We solve the system of differential equations (5) numerically using the standard finite-element package COMSOL MULTIPHYSICS [38].

Figure 2(a) shows the energy levels as a function of the dot radius R for three angular momenta, $m = -1, 0, 1$ at K valley for zero magnetic field. The spectrum shows a band gap between the valence and conduction bands which closes as the dot radius increases. We found that the lowest electron state in Fig. 2(a) exhibits an $\sim 1/R^3$ dependency at low energies ($E \lesssim t/2$) and $\sim 1/R$ dependency at high energies ($E \gtrsim t/2$) [see Fig. 2(b)]. This behavior can be linked to the fact that the lowest energy band in a TLG is described by $E(k) \sim k^3$ at low energies which turns into a linear spectrum $E(k) \sim k$ at high energies. This is in contrast with BLG QD in which the lowest energy level shows an $\sim 1/R^2$ dependency [19] which is a consequence of the quadratic energy dispersion, i.e., $E(k) \sim k^2$, of BLG. The energy levels exhibit anticrossings near the interlayer coupling energy in TLG, i.e., $t \approx 400$ meV. Notice that the energy levels in Fig. 2(a) are twofold degenerate due to the valley symmetry. This degeneracy occurs between the $E_K(m)$ and $E_{K'}(-(m+1))$ states. Furthermore, the energy levels in Fig. 2(a) exhibit $E_K(m) = -E_{K'}(m)$ symmetry between the electron and hole states. In Fig. 3(a) the energy levels corresponding to $m = -1$ for both the K and K' valleys are plotted.

IV. TLG QD: NONZERO MAGNETIC FIELD

In the presence of a perpendicular magnetic field $\vec{B} = B\hat{z}$, the canonical momentum $\vec{p} = (p_x, p_y)$ is replaced by the gauge-invariant kinetic momentum $\vec{p} + e\vec{A}(\vec{r})$ with the vector potential in the symmetric gauge $\vec{A}(\vec{r}) = (0, Br/2, 0)$. Therefore, the operators π and $\pi^\dagger$ in the Hamiltonian (1) are described in polar coordinates by

$$\pi = -i\hbar v_F e^{i\theta}\left[\frac{\partial}{\partial r} + \frac{i}{r}\frac{\partial}{\partial \theta} - \frac{eBr}{2\hbar}\right], \quad (22)$$

$$\pi^\dagger = -i\hbar v_F e^{-i\theta}\left[\frac{\partial}{\partial r} - \frac{i}{r}\frac{\partial}{\partial \theta} + \frac{eBr}{2\hbar}\right], \quad (23)$$

and the radial dependence of the wave components becomes (for $\Delta' = 0$)

$$\left[\frac{\partial}{\partial \rho} - \frac{m-1}{\rho} - \beta\rho\right]\phi_{B1}(\rho) = \varepsilon\phi_{A1}(\rho) - t'\phi_{B2}(\rho),$$

$$\left[\frac{\partial}{\partial \rho} + \frac{m}{\rho} + \beta\rho\right]\phi_{A1}(\rho) = -\varepsilon\phi_{B1}(\rho),$$

$$\left[\frac{\partial}{\partial \rho} + \frac{m+1}{\rho} + \beta\rho\right]\phi_{A2}(\rho) = \varepsilon\phi_{B2}(\rho) - t'\phi_{A1}(\rho),$$

$$\left[\frac{\partial}{\partial \rho} - \frac{m}{\rho} - \beta\rho\right]\phi_{B2}(\rho) = -\varepsilon\phi_{A2}(\rho) + t'\phi_{B3}(\rho),$$

$$\left[\frac{\partial}{\partial \rho} - \frac{m+1}{\rho} - \beta\rho\right]\phi_{B3}(\rho) = \varepsilon\phi_{A3}(\rho),$$

$$\left[\frac{\partial}{\partial \rho} + \frac{m+2}{\rho} + \beta\rho\right]\phi_{A3}(\rho) = -\varepsilon\phi_{B3}(\rho) + t'\phi_{A2}(\rho),$$

(24)

where $\beta = eBR^2/2\hbar = R^2/l_B^2$ and $l_B = \sqrt{\hbar/eB}$ is the magnetic length.

Figure 3(b) depicts the energy levels calculated numerically as a function of dot radius R. For comparison with the results
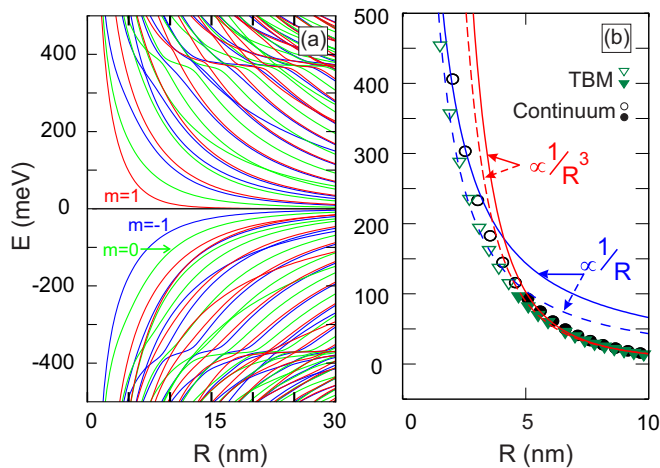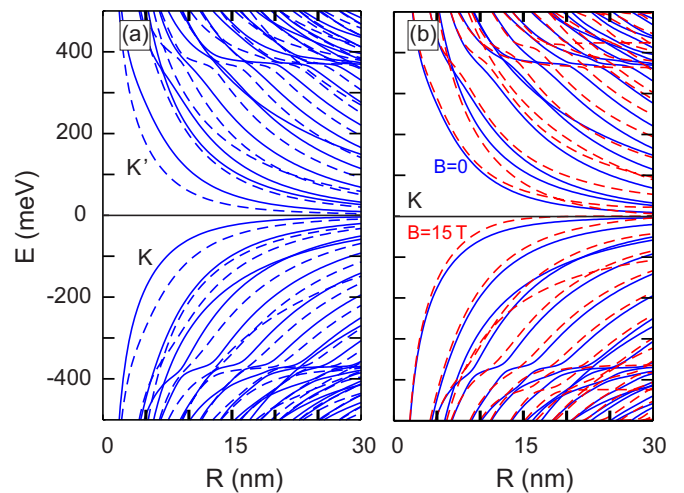

FIG. 2. (a) Energy levels in the absence of magnetic field as a function of dot radius R, for three different angular momenta $m = -1$ (blue), $m = 0$ (green), $m = 1$ (red) at the K valley. (b) Lowest electron state obtained within the continuum model (circles) and the TBM (triangles) which is fitted to an $\sim \alpha/R$ function (blue curves) at small radii (open symbols) and to an $\sim \beta/R^3$ function (red curves) at large radii (full symbols). Solid (dashed) curves indicate fitting to the continuum (TBM) data and α, β are the fitting parameters.

FIG. 3. Energy levels as a function of dot radius R, for a particular angular momentum $m = -1$: (a) at the two valleys K (solid curves) and K' (dashed curves) in the absence of magnetic field, $B = 0$. The spectrum exhibits the symmetry $E_K(m) = -E_{K'}(m)$. (b) Energy spectrum at the valley K in the absence (blue solid curves) and presence (red dashed curves) of the magnetic field, $B = 15$ T.
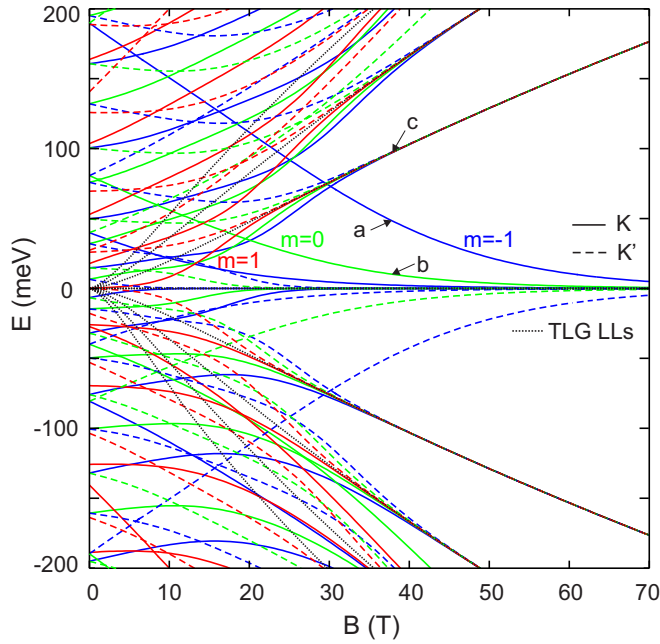
FIG. 4. Energy spectrum as a function of magnetic field B, for dot radius $R = 25$ nm and $m = -1$ (blue), $m = 0$ (green), $m = 1$ (red) at the two valleys K (solid curves) and K' (dashed curves). Gray dotted curves depict the TLG LLs.

of zero magnetic field, we plot the energy levels as function of R in the absence (blue solid curves) and presence (red dashed curves) of the magnetic field for $m = -1$, at the K valley.

The dependence of the spectrum on magnetic field for the two valleys K (solid curves) and K' (dashed curves) are shown in Fig. 4. The results are presented for $m = -1$ (blue), $m = 0$ (green), and $m = 1$ (red) with the dot radius $R = 25$ nm. Energy spectrum shows the symmetry $E_K(m) = -E_{K'}(m)$ for the electron and hole states which also holds in the zero magnetic field case. As we can see, at $B = 0$, the energy levels for $m = -1$ and $m = 0$ are degenerate with different valley indexes, i.e., $E_{K(K')}(-1) = E_{K'(K)}(0)$. For $B \neq 0$ this degeneracy and the symmetry condition $E_K(m) = E_{K'}(-(m+1))$ is no longer preserved. At high magnetic fields, i.e., $l_B \ll R$, the carriers become localized at the center of the dot and the energy levels merge into the Landau levels (LLs) of TLG. The gray dotted curves in Fig. 4 show the LLs of TLG [29–31]. The states with $m \leq 0$ in both valleys form the zero-energy ($n = 0$) LL in the conduction and valence bands. This is different from the previous studies of MLG QD [27] and BLG QD [21] with infinite-mass boundary condition in which only one of the valleys contributes to the zero LL in each band.

The probability density for each sublattice $A1, \ldots, B3$ (upper panels) and each layer (lower panels) corresponding to the points labeled by (a), (b), and (c) in Fig. 4, are shown in Figs. 5(a), 5(b), and 5(c), respectively. The figures are plotted for $R = 25$ nm and $B = 37.77$ T. At the point (a) with $m = -1$ and $E_K = 48.55$ meV, most of the probability density belongs to the sublattices $B1$ and $B2$ with the main confinement spread out over the dot. On the other hand, confinement for the sublattice $A1$ takes place near $\rho = 1$. At
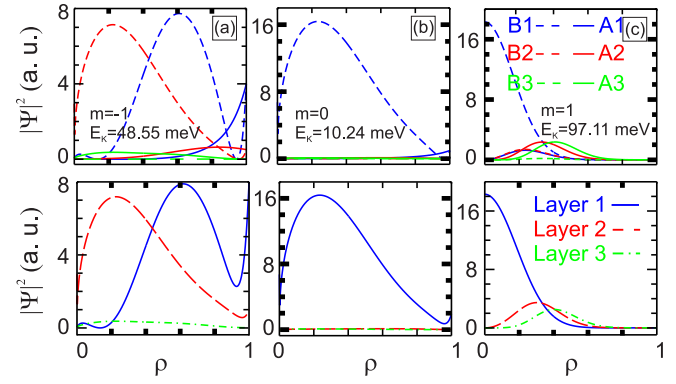

FIG. 5. Probability density on the different sublattices (upper panels) and on the different layers (lower panels) for (a) $m = -1$, (b) $m = 0$, and (c) $m = 1$ at the respective points shown in the energy spectrum of Fig. 4 with dot radius $R = 25$ nm and magnetic field $B = 37.77$ T. Layer 1 (2, 3) is represented by the blue solid (red dashed, green dot-dashed) curves. Sublattices $A1$, $A2$, and $A3$ ($B1$, $B2$, and $B3$) are respectively represented by the blue, red, and green solid (dashed) curves.

point (b) ($m = 0$, $E_K = 10.24$ meV) the electron is mostly confined at sublattice B_1 and in layer 1 [see Fig. 5(b)]. The $A1 - B2$ and $A2 - B3$ sites, which mutually stack right on top of each other (dimer sites), become occupied at high energies (compared to the energy scale $t \approx 400$ meV). For the energy state (c) the electrons are confined deep inside the dot, far away from the boundary, since this state coincides with the first LL and the electrons are strongly localized at the center of the dot. Unlike layer 1 where the wave function is centered around $\rho = 0$, in layers 2 and 3 the wave functions form rings with maximum at $\rho \neq 0$ and with lower probability density compared to layer 1 (see lower panels).

V. COMPARISON WITH TIGHT BINDING

In order to check the validity of the continuum approximation, we compare our analytical results with the energy levels calculated within a nearest-neighbor tight-binding approach. Besides, such comparison is interesting due to the fact that the tight-binding results allow us to study TLG QDs with realistic edges and observe in this way the effect of edges on the energy levels of TLG QDs. The tight-binding Hamiltonian of TLG [32–36] can be described by

$$\mathcal{H}_{TB} = \sum_{m \neq n} (\tau_{mn} c_m^{\dagger} c_n + \text{H.c.}) + \sum_m (\epsilon_m + \Delta_m) c_m^{\dagger} c_m, \quad (25)$$

where c_m ($c_m^{\dagger}$) annihilates (creates) an electron in site m with on-site energy ϵ_m. The sum is taken only between the nearest-neighbor atoms and τ_{mn} is the hopping parameter, with $\tau_{mn} = t_0 = 2.7$ eV ($\tau_{mn} = t = 0.4$ eV) being the intralayer (interlayer) hopping contributions. In ABC-stacked TLG, the atoms in the A (B) sublattice in a certain layer are linked with the B (A) sublattice in the other layer [33,39] [see Fig. 1(a) and the inset in Fig. 6(b)]. Δ_m is the on-site mass potential term. Recently, it has been experimentally [40–42] shown and theoretically [43] demonstrated that by inducing an interaction with an appropriate substrate, one can open a gap
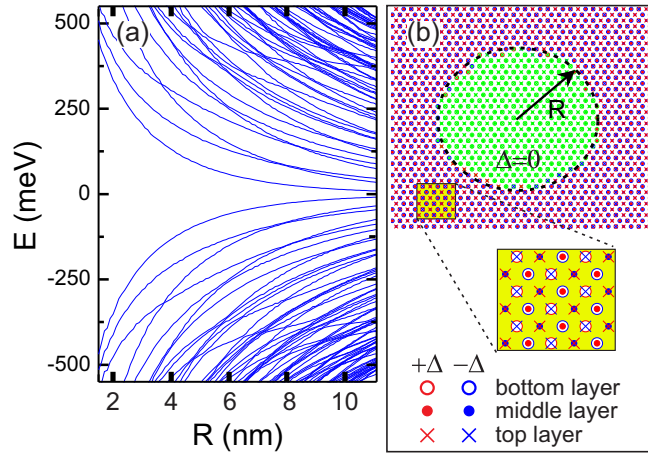
FIG. 6. (a) Energy levels as a function of dot radius R, obtained via the tight-binding model in the absence of magnetic field. (b) Sketch of the QDs defined by a site-dependent staggered potential Δ_i, where the atoms belonging to sublattices $A_{1,2,3}$ ($B_{1,2,3}$) have a mass-term potential given by $+\Delta$ ($-\Delta$), respectively, and $\Delta_i = 0$ in the region inside the dot, represented in green. Bottom, middle, and top atoms are given by open, full, and ×-like symbols, respectively.

in the energy spectrum of graphene [44] and, consequently, simulate electronic confinement in graphene nanostructures and quantum devices [8,43,45–47].

Here, the QD is surrounded by a staggered site-dependent potential such that $\Delta_m = +\Delta$ ($\Delta_m = -\Delta$) if m belongs to sublattice A (B). This simulates the substrate effect which breaks the sublattice symmetry of the system [22,47,48]. In Fig. 6(b) we show how such QD structure is arranged, presenting the atomic positions and their respective mass-potential amplitudes, with $\Delta_m = 0$ inside the dot region represented in green, and red (blue) for $\Delta_m > 0$ ($\Delta_m < 0$) outside the QD, respectively. The effect of an external magnetic field is incorporated in the tight-binding model by including a phase in the hopping parameters via the Peierls substitution, as $\tau_{mn} \to \tau_{mn} \exp\left[i\frac{e}{\hbar}\int_n^m \vec{A}\cdot\vec{dl}\right]$, where $\vec{A}$ is the vector potential [22,47]. For an external magnetic field perpendicular to the TLG flakes, $\vec{B} = B\hat{z}$, we conveniently choose the Landau gauge $\vec{A} = (0, Bx, 0)$, and thus we find that the Peierls phase is only nonzero in the y direction, given by $\exp\left[i\frac{\sqrt{3}eax}{2\hbar}B\right]$, where $a = 0.142$ nm is the graphene lattice parameter. Writing the Hamiltonian $\mathcal{H}_{TB}$ in a matrix form, we diagonalize the matrix numerically and obtain the energy levels of the studied TLG QDs.

Figure 6(a) shows the energy levels of circular TLG QDs defined by a very large mass-term potential of $\Delta = 1.0$ eV as a function of the QD radius. It looks qualitatively similar to the one shown in Fig. 2(a) for the spectra obtained within the continuum approach. Note that the angular momentum indices m are indistinguishable in the tight-binding approach, different from the continuum case, such that we cannot *a priori* identify them in order to perform a direct comparison between the results for each individual energy level of both models. Similar to the continuum results, the tight-binding energy spectrum [Fig. 6(a)] depicts the following features: (*i*) it preserves the electron-hole symmetry $E_e = -E_h$, (*ii*) the
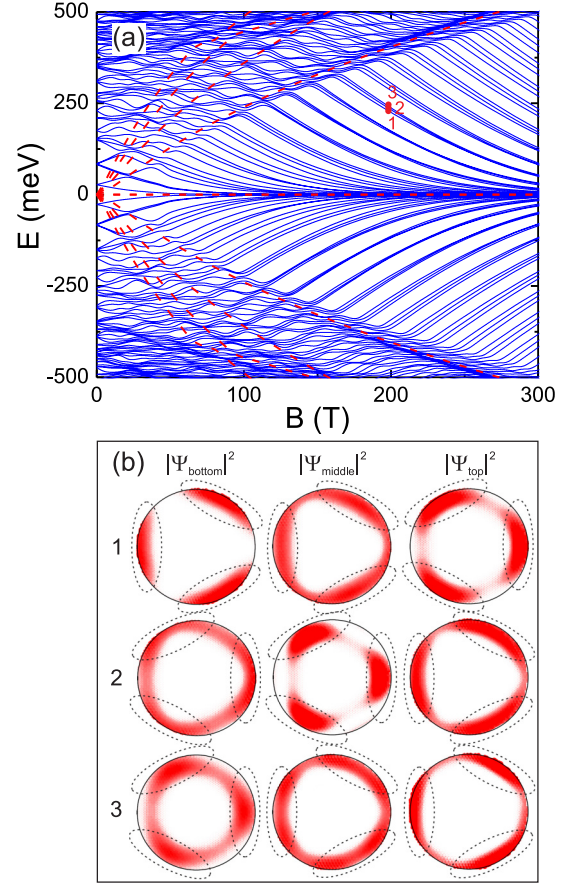

FIG. 7. (a) Energy spectrum of a circular TLG QD defined by a site-dependent staggered potential as a function of a perpendicular magnetic field with $R = 8$ nm obtained within the tight-binding model. The red dashed curves are the four first LLs of bulk TLG. (b) The probability amplitude for the bottom ($|\Psi_{\text{bottom}}|^2$), middle ($|\Psi_{\text{middle}}|^2$), and top ($|\Psi_{\text{top}}|^2$) graphene layers are shown for a group of three quantum Hall edge states labeled by points 1 ($E \approx 230.18$ meV), 2 ($E \approx 237.74$ meV), and 3 ($E \approx 242.90$ meV) indicated in (a) at the magnetic field $B \approx 203$ T. Shiny red represents higher-density amplitudes.

energy gap between the electron and hole states decreases when the QD radius increases, and (*iii*) the energy levels exhibit anticrossings close to the interlayer hopping energy value, i.e., $t \approx 400$ meV. Similar to the continuum model, the lowest electron energy level shows an $\sim 1/R^3$ and $\sim 1/R$ dependency at low and high energies, respectively [see Fig. 2(b)]. Similar to the continuum results, the energy levels in Fig. 6(a) are twofold degenerate due to the valley symmetry in the absence of magnetic field.

The tight-binding energy levels for a circular TLG QD defined by a site-dependent mass potential with radius $R = 8$ nm as a function of a perpendicular magnetic field is shown in Fig. 7(a). Equivalent to MLG [8,27,28] and BLG QDs [19,22] defined by a mass-potential media, the TLG QD magnetic energy levels approach the LLs of an infinite TLG sheet [29–31,39] (shown by the dashed red curves in the spectrum) as B increases. The magnetic spectrum obtained via the tight-binding model [Fig. 7(a)] is qualitatively comparable with

the one obtained using the continuum model (Fig. 4). The energy levels in both spectra exhibit similar magnetic field dependences and approach the LLs of an infinite TLG sheet. In comparison with the circular QD spectrum defined by a mass-potential media for MLG [8,27,28] and BLG [19,22], we observe some interesting similar and different features. From Fig. 7, one can enumerate the following similarities: (*i*) the TLG QD energy spectrum exhibits electron-hole symmetry $E_e = -E_h$, (*ii*) degeneracies are lifted in the presence of the magnetic field resulting in many more energy levels, and (*iii*) the spectrum displays a small energy gap between the electron and hole states at low magnetic fields that decreases as the magnetic field increases. And the differences are as follows. (*i*) As the magnetic flux increases, groups of three energy levels are decreasing in energy and approach the zero LL (i.e., $E = 0$). Notice that these groups of states have very close energies but are nondegenerate. It has been reported that for MLG [8,27,28] and BLG QDs [19,22] with mass-potential confinement, these groups are formed by just one and two states, respectively. This is linked to the layer symmetry where we have three graphene layers and, consequently, a group of three quantum Hall edge states. (*ii*) A bunch of anticrossings are found for energies higher than the first LL, whereas the energy levels corresponding to the monolayer and bilayer cases exhibit crossings. This is a consequence of the mixing of the states of K and K' valleys due to the combination of both armchair and zigzag edges at the circular boundary of the TLG QD [19].

Figure 7(b) shows the corresponding electron densities for a group of three quantum Hall edge states, labeled by points 1, 2, and 3 in Fig. 7(a) at the magnetic field $B \approx 203$ T. The electron densities for the bottom ($|\Psi_{\text{bottom}}|^2$), middle ($|\Psi_{\text{middle}}|^2$), and top ($|\Psi_{\text{top}}|^2$) layers are shown separately. Due to the layer symmetry in TLG QDs, the wave functions in each layer can be transformed into each other by a $2\pi/3$ rotation and thus the total probability densities for states labeled by 1, 2, and 3 remain with the same symmetry and shape.

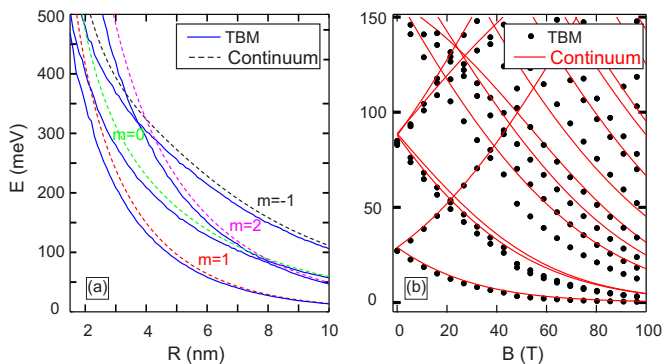In Figs. 8 we compare the results of the continuum and TB approaches for the lowest energy levels of a circular TLG QD as a function of (a) radius R and (b) magnetic field B at fixed $R = 8$ nm. We find the following. (*i*) In the absence of B the lowest energy levels in both methods approach each other as the dot size increases [see Fig. 8(a)]. This is due to the fact that for large sizes the approximation of the continuum model, which basically is valid for low energy of an infinite TLG sheet, becomes more accurate. (*ii*) For $B \neq 0$ we find that the lowest electron state obtained within the continuum model is in excellent agreement with the TBM result. For the higher energy levels, the discrepancy between the continuum and TBM results becomes more significant resulting from (a) the lower accuracy of the continuum model at high energies and (b) the different boundary condition, i.e., in the TB approach the boundary is not a perfect circle due to the discreteness of the lattice.

VI. CONCLUSIONS

In summary, we presented analytical and numerical calculations, based on continuum and tight-binding models, for the confined states in ABC-stacked TLG QD created by a mass term potential in the presence and in the absence of an external magnetic field. By using the continuum approximation, we first derived the infinite-mass boundary conditions for TLG and applied these boundary conditions for circular QDs in TLG. The mass-potential media is included in both models in order to break locally the sublattice symmetry of the system and, consequently, to open a gap in the carrier energy spectrum. Such a mass-potential can be realized experimentally using an appropriate nanostructured substrate for TLG and is modeled in the tight-binding description by a staggered site-dependent potential.

By comparing the analytical results obtained in the continuum approximation with the tight-binding ones for a circular TLG QD, we found good agreement between both methods at low energy and they show qualitative similar behaviors for the confined states. By analyzing the energy states and the corresponding wave functions, we investigated the electronic features of the TLG QDs spectra, showing the main similarities and differences with respect to QDs defined in MLG and BLG.

Our theoretical results show the following. (*i*) The energy spectra exhibit the intervalley symmetry $E_K^e(m) = -E_{K'}^h(m)$ and electron-hole symmetry $E_e = -E_h$ is preserved in both approaches. For both methods such symmetries were observed both in the absence and in the presence of a perpendicular magnetic field. (*ii*) By increasing the magnetic field, the energy levels of a circular TLG QD approach the LLs of an infinite ABC-stacked TLG sheet. (*iii*) A magnetic field breaks the degeneracy of the confined energy states. (*iv*) The zero-energy LL in the spectrum obtained in the continuum approach is formed by the magnetic states with $m \leq 0$ for both Dirac valleys. (*v*) The quantum Hall edge states in the tight-binding magnetic spectrum approach the zero LL of an infinite TLG in groups of three states, which results from the layer symmetry in TLG QDs.

Comparing TBM and continuum results in both $B = 0$ and $B \neq 0$, we found good agreement between both approaches for the low energy levels. This agreement is an additional confirmation of our derivation of the infinite-mass boundary condition in TLG.

FIG. 8. (a) Lowest electron energy levels as a function of dot radius, R, calculated within the continuum model (dashed curves) and the TBM (blue solid curves) for $B = 0$. (b) The lowest electron energy spectrum as a function of magnetic field obtained using the continuum model (red solid curves) and the TBM (black circles) with $R = 8$ nm.

In addition to the ABC-stacked TLG, the ABA-stacked is also favorable in TLG. The lowest energy bands of ABA-stacked TLG consist of two linear MLG-like bands and four massive BLG-like bands [29] which implies slightly different electronic properties than ABC-stacked TLG. This motivates a future study of energy levels of QDs in an ABA-stacked TLG.

[1] A. D. Güçlü, P. Potasz, M. Korkusinski, P. Hawrylak, X. Li, S. P. Lau, L. Tang, R. Ji, and P. Yang, *Graphene Quantum Dots* (Springer, New York, 2014).

[2] A. V. Rozhkov, G. Giavaras, Y. P. Bliokh, V. Freilikher, and F. Nori, Phys. Rep. **503**, 77 (2011).

[3] A. V. Rozhkov and F. Nori, Phys. Rev. B **81**, 155401 (2010).

[4] P. Recher and B. Trauzettel, Nanotechnology **21**, 302001 (2010).

[5] J. Guttinger, T. Frey, C. Stampfer, T. Ihn, and K. Ensslin, Phys. Rev. Lett. **105**, 116801 (2010).

[6] M. Ezawa, Phys. Rev. B **76**, 245415 (2007).

[7] B. Trauzettel, D. V. Bulaev, D. Loss, and G. Burkard, Nat. Phys. **3**, 192 (2007).

[8] S. Schnez, K. Ensslin, M. Sigrist, and T. Ihn, Phys. Rev. B **78**, 195427 (2008).

[9] Z. Z. Zhang, K. Chang, and F. M. Peeters, Phys. Rev. B **77**, 235411 (2008).

[10] M. Zarenia, A. Chaves, G. A. Farias, and F. M. Peeters, Phys. Rev. B **84**, 245403 (2011).

[11] G. Giavaras and F. Nori, Appl. Phys. Lett. **97**, 243106 (2010).

[12] L. A. Ponomarenko, F. Schedin, M. I. Katsnelson, R. Yang, E. H. Hill, K. S. Novoselov, and A. K. Geim, Science **320**, 356 (2008).

[13] T. Ihn, J. Güttinger, F. Molitor, S. Schnez, E. Schurtenberger, A. Jacobsen, S. Hellmüller, T. Frey, S. Dröscher, C. Stampfer, and K. Ensslin, Mater. Today **13**, 44 (2012).

[14] J. M. Pereira, P. Vasilopoulos, and F. M. Peeters, Nano Lett. **7**, 946 (2007).

[15] J. M. Pereira, Jr., F. M. Peeters, P. Vasilopoulos, R. N. Costa Filho, and G. A. Farias, Phys. Rev. B **79**, 195403 (2009).

[16] A. D. Güçlü, P. Potasz, and P. Hawrylak, Phys. Rev. B **84**, 035425 (2011).

[17] D. P. Zebrowski, E. Wach, and B. Szafran, Phys. Rev. B **88**, 165405 (2013).

[18] M. T. Allen, J. Martin, and A. Yacoby, Nat. Commun. **3**, 934 (2012).

[19] D. R. da Costa, M. Zarenia, A. Chaves, G. A. Farias, and F. M. Peeters, Carbon **78**, 392 (2014).

[20] M. Zarenia, B. Partoens, T. Chakraborty, and F. M. Peeters, Phys. Rev. B **88**, 245432 (2013).

[21] D. R. da Costa, M. Zarenia, A. Chaves, G. A. Farias, and F. M. Peeters, Phys. Rev. B **92**, 115437 (2015).

[22] D. R. da Costa, M. Zarenia, A. Chaves, G. A. Farias, and F. M. Peeters, Phys. Rev. B **93**, 085401 (2016).

[23] C.-J. Shih, A. Vijayaraghavan, R. Krishnan, R. Sharma, J.-H. Han, M.-H. Ham, Z. Jin, S. Lin, G. L. C. Paulus, N. F. Reuel, Q. H. Wang, D. Blankschtein, and M. S. Strano, Nat. Nanotechnol. **6**, 439 (2011).

[24] G. Tsoukleri, J. Parthenios, C. Galiotis, and K. Papagelis, 2D Mater. **2**, 024009 (2015).

[25] M. V. Berry and R. J. Modragon, Proc. R. Soc. London A **412**, 53 (1987).

[26] M. Zarenia, J. M. Pereira, A. Chaves, F. M. Peeters, and G. A. Farias, Phys. Rev. B **81**, 045431 (2010).

[27] M. Grüjić, M. Zarenia, A. Chaves, M. Tadić, G. A. Farias, and F. M. Peeters, Phys. Rev. B **84**, 205441 (2011).

[28] M. Ramezani Masir, A. Matulis, and F. M. Peeters, Phys. Rev. B **84**, 245413 (2011).

[29] S. Yuan, R. Roldán, and M. I. Katsnelson, Phys. Rev. B **84**, 125455 (2011).

[30] S. H. R. Sena, J. M. Pereira, F. M. Peeters, and G. A. Farias, Phys. Rev. B **84**, 205448 (2011).

[31] S. H. R. Sena, J. M. Pereira, Jr., G. A. Farias, and F. M. Peeters, Phys. Rev. B **86**, 085412 (2012).

[32] C. L. Lu, C. P. Chang, Y. C. Huang, R. B. Chen, and M. L. Lin, Phys. Rev. B **73**, 144427 (2006).

[33] F. Zhang, B. Sahu, H. Min, and A. H. MacDonald, Phys. Rev. B **82**, 035409 (2010).

[34] M. Koshino and T. Ando, Phys. Rev. B **76**, 085425 (2007).

[35] M. F. Craciun, S. Russo, M. Yamamoto, J. B. Oostinga, A. F. Morpurgo, and S. Tarucha, Nat. Nanotechnol. **4**, 383 (2009).

[36] H. Min and A. H. MacDonald, Prog. Theor. Phys. Suppl. **176**, 227 (2008).

[37] A. K. Geim and I. V Grigorieva, Nature (London) **499**, 419 (2013).

[38] For more details, see the COMSOL MULTIPHYSICS website: http://www.comsol.com.

[39] W. Bao, L. Jing, J. Velasco, Jr., Y. Lee, G. Liu, D. Tran, D. Smirnov, M. Koshino, E. McCann, M. Bockrath, and C. N. Lau, Nat. Phys. **7**, 948 (2011).

[40] S. Y. Zhou, G.-H. Gweon, A. V. Fedorov, P. N. First, W. A. de Heer, D.-H. Lee, F. Guinea, A. H. Castro Neto, and A. Lanzara, Nat. Mater. **6**, 770 (2007).

[41] M. S. Nevius, M. Conrad, F. Wang, A. Celis, M. N. Nair, A. Taleb-Ibrahimi, A. Tejeda, and E. H. Conrad, Phys. Rev. Lett. **115**, 136802 (2015).

[42] W.-X. Wang, L.-J. Yin, J.-B. Qiao, T. Cai, S.-Y. Li, R.-F. Dou, J.-C. Nie, X. Wu, and L. He, Phys. Rev. B **92**, 165420 (2015).

[43] G. Giovannetti, P. A. Khomyakov, G. Brocks, P. J. Kelly, and J. van den Brink, Phys. Rev. B **76**, 073103 (2007).

[44] J. Wurm, A. Rycerz, I. Adagideli, M. Wimmer, K. Richter, and H. U. Baranger, Phys. Rev. Lett. **102**, 056806 (2009).

[45] C. R. Dean, A. F. Young, I. Meric, C. Lee, L. Wang, S. Sorgenfrei, K. Watanabe, T. Taniguchi, P. Kim, K. L. Shepard, and J. Hone, Nat. Nanotechnol. **5**, 722 (2010).

[46] P. Recher, B. Trauzettel, A. Rycerz, Ya. M. Blanter, C. W. J. Beenakker, and A. F. Morpurgo, Phys. Rev. B **76**, 235404 (2007).

[47] D. R. da Costa, A. Chaves, M. Zarenia, J. M. Pereira, Jr., G. A. Farias, and F. M. Peeters, Phys. Rev. B **89**, 075418 (2014).

[48] M. Zarenia, O. Leenaerts, B. Partoens, and F. M. Peeters, Phys. Rev. B **86**, 085451 (2012).